Geophysical Journal International

Geophys. J. Int. (2021) **224,** 1621–1639
Advance Access publication 2020 November 13
GJI Marine Geosciences and Applied Geophysics

doi: 10.1093/gji/ggaa543

Reflection of inhomogeneous plane waves at the surface of a thermo-poroelastic medium

Enjiang Wang,[1,2] José M. Carcione,[3,4] Yang Yuan[5] and Jing Ba[3]

[1] *Key Lab of Submarine Geosciences and Prospecting Techniques, MOE, College of Marine Geosciences, Ocean University of China, Qingdao* 266100, *China*
[2] *Evaluation and Detection Technology Laboratory of Marine Mineral Resources, Qingdao National Laboratory for Marine Science and Technology, Qingdao* 266061, *China*
[3] *School of Earth Sciences and Engineering, Hohai University, Nanjing* 211100, *China. E-mail: jba@hhu.edu.cn*
[4] *National Institute of Oceanography and Applied Geophysics - OGS, Trieste* 34010, *Italy*
[5] *CNOOC China Limited, ShenZhen Branch, Shenzhen* 518000, *China*

Accepted 2020 November 12. Received 2020 October 20; in original form 2020 July 6

SUMMARY

We analyse the reflection coefficient of an inhomogeneous plane wave incident on the thermally insulated surface of a thermo-poroelastic medium. The theory, which includes the classic Lord-Shulman (LS) and Green-Lindsay (GL) theories as well as a generalization of the LS model, predicts three inhomogeneous longitudinal waves and one transverse wave, described by potential functions specified by the propagation direction and inhomogeneity angle. The GL model can give a stronger P1-wave thermal attenuation and consequently a stronger velocity dispersion than the LS model. We investigate the influence of inhomogeneity angle, type of incident wave, frequency and surface boundary conditions. The generalized LS model exhibits increased P1-wave thermal attenuation with increasing Maxwell–Vernotte–Cattaneo relaxation time and consequently predicts more interference energy, irrespective if the surface is open or sealed. The inhomogeneity angle affects the energy partitions particularly near the grazing incidence, with a significant interference energy, which must be taken into account to satisfy the energy conservation. The thermal dispersion occurs at frequencies around the thermal relaxation peak, which moves to low frequencies when the conductivity increases.

Key words: Elasticity and anelasticity; Numerical modelling; Seismic attenuation; Wave propagation.

1 INTRODUCTION

Wave propagation in fluid-saturated high-pressure high-temperature fields, such as geothermal reservoirs, is affected by both the porous nature of rocks and their thermal properties (e.g. Poletto *et al.* 2018; Carcione *et al.* 2019b). A quantitative investigation of wave propagation in such fields, including reflections from the discontinuity interface is important to infer the medium properties, such as permeability, porosity and thermal conductivity. This problem is relevant in a variety of fields, such as mechanics, thermodynamics, chemical engineering, and geothermal and hydrocarbon exploration (Deresiewicz 1960; Sharma *et al.* 2003; Wei *et al.* 2016; Sharma 2018).

Biot (1956a, 1962) considered a medium saturated by a single viscous fluid and established the fundamental constitutive relations. The theory predicts two compressional (*P*) waves and one shear wave. The second *P* wave is diffusive at low frequencies and wave-like at high frequencies. This theory has been widely applied to study the reflection/transmission problem at various interfaces, including the contact between two porous media (Deresiewicz & Rice 1964; Dutta & Odé 1983; Gurevich *et al.* 2004), a fluid/porous solid interface (Santos *et al.* 1992), and a layer of viscous fluid bounded by two porous saturated half-spaces (Markov *et al.* 2019).

The classical Biot theory cannot explain the high level of attenuation at the seismic frequency band. Many generalizations have been developed, including two fluids (Santos *et al.* 1990; Lo *et al.* 2005), two solids (Carcione & Seriani 2001; Santos *et al.* 2004), and double porosity (Pride *et al.* 2004; Ba *et al.* 2011, 2017). One of these models assumes that the porous medium consists of a frame saturated by two immiscible fluids (Santos *et al.* 1990; Lo *et al.* 2005) and predicts an additional highly attenuated *P* wave. On the basis of this model, the reflection and transmission coefficients at the interface between elastic and porous media (Tomar & Arora 2006), and two porous media (Kumar & Sharma 2013) were investigated. Carcione & Seriani (2001) considered a composite two-mineral rock saturated by a single fluid. The theory predicts three *P* waves and two *S* waves, and has been further generalized to the non-uniform porosity case (Carcione *et al.* 2003;

Santos *et al.* 2004). Using this theory, Rubino *et al.* (2006) investigated the energy reflection and transmission at the interface between two composite porous media. Pride & Berryman (2003a,b) proposed a double-porosity model, where the coupling between the rock deformation and the mesoscopic local fluid flow (LFF) is introduced. This theory is an effective Biot model, and is used to obtain the reflection coefficient at the interface between two porous media (Zhao *et al.* 2015), and the reflection of an inhomogeneous wave at the free surface (Liu *et al.* 2020b). By combining the Rayleigh model of bubble oscillations with Biot theory of poroelasticity, Ba *et al.* (2011) proposed a double-porosity model, where the process of wave-induced LFF is described by the liquid collapse on a spherical cavity. Sharma (2013) used this theory to analyse the wave reflection at the free surface, while Wang *et al.* (2020) solved the reflection/transmission at the interface between two double-porosity media. Guo & Gurevich (2020a,b) considered the coupling between wave-induced fluid flow and elastic scattering and studied the frequency-dependent *P*-wave dispersion and attenuation anisotropy in rocks with aligned fractures.

On the other hand, thermoelastic attenuation is analogous to poroelastic attenuation, due to the conversion of the fast *P* wave to the thermal wave (Carcione *et al.* 2020). Biot (1956b) pioneered the study and established a parabolic-type differential equation based on the classical heat conduction theory, but it predicts unphysical solutions as a function of frequency, such as infinite velocities. Lord & Shulman (1967) formulated more physical differential equations by adopting a hyperbolic-type heat equation involving a single relaxation time. This theory yields a Maxwell-type attenuation kernel and predicts a wave-like propagation (finite velocity) at high frequencies. Green & Lindsay (1972) used two relaxation times in the constitutive relations and proposed a different generalization. These theories predict two *P* waves and an *S* wave. The second *P* wave is diffusive at low frequencies and wave-like at high frequencies (Rudgers 1990; Carcione *et al.* 2019b), in analogy with the slow *P* wave of poroelasticity. Using the thermoelasticity theory, Deresiewicz (1957) performed a plane-wave analysis and studied the effect of boundaries on the reflection by stress-free boundary (1960). Sinha & Elsibai (1996) studied the reflection of thermoelastic waves at the free surface of a solid half-space in the context of the generalized theory with two relaxation times. A similar problem was investigated by Sharma *et al.* (2003), and Kumar & Sarthi (2006) discussed the reflection and refraction of plane waves at an interface between two thermoelastic media, but assumed no energy dissipation. Singh & Chakraborty (2013) studied the effects of initial stress on the reflection and refraction coefficients of thermoelastic waves at a solid-liquid interface. More recently, Carcione *et al.* (2019b) proposed a numerical method for simulating wave propagation in heterogeneous thermoelastic media based on the Fourier differential operator and an explicit Crank-Nicolson time-integration method.

The thermo-poroelasticity theory describes the couplings between the stress components and the temperature field in porous media (Sharma 2008; Carcione *et al.* 2019a). The dynamical equations predict three *P* waves, namely, a fast *P* wave, a slow Biot wave, and a slow *T* (thermal) wave. The two slow waves present a diffusive behaviour under certain conditions, depending on the viscosity, frequency, and thermoelasticity constants (Sharma 2008). Carcione *et al.* (2019a) derived a system of thermo-poroelasticity equations by combining Biot equations of poroelasticity with those of Lord & Shulman (1967), and numerically solved it using a direct-grid algorithm. Wei *et al.* (2016) studied the reflection and refraction at the interface between thermoelastic and thermo-poroelastic media, where the incident wave is lossless, which is an approximation in the presence of thermal and fluid-related diffusion. Sharma (2018) studied the same problem but considered an incident inhomogeneous wave.

A quantitative investigation of reflection at the surface of a thermo-poroelastic medium is important to understand the wave-propagation effects. Since until now the subject has not been studied in detail, we consider a generalized medium described by a unified theory that includes the classical LS and GL models, depending on the relaxation times involved. Moreover, we consider further generalization of the LS model by using different values of the Maxwell–Vernotte–Cattaneo (MVC) relaxation times. The plane-wave solutions are based on Helmholtz potential functions, and frequency-dependent phase velocities and dissipation factors are obtained. The conversion from fast wave to slow and thermal waves induces energy losses and wave inhomogeneity, which means that the propagation and attenuation directions do not coincide (Buchen 1971; Carcione 2006; Liu *et al.* 2020a). We consider an incident inhomogeneous wave based on the complex velocity, and propagation and inhomogeneity angles. The reflection coefficients and energy partitions due to an obliquely incident wave are obtained in closed form, on the basis of the boundary conditions at the surface. The examples illustrate the reflection characteristics, as a function of the incidence angle, inhomogeneity angle, the frequency, and the type of incident wave. The results are compared with those of the Biot theory to highlight the thermal effects, depending on the thermal mechanism (LS or GL) and thermal properties.

2 GENERAL THERMO-POROELASTICITY THEORY

The thermo-poroelasticity theory combines the equation of heat conduction with Biot's equations of poroelasticity. It describes wave propagation in thermally conducting porous media saturated with a viscous fluid. In the following, the generalized equations including both the LS and GL models are established and the corresponding plane-wave response is analysed.

2.1 Basic equations

Considering a 2D isotropic medium, let us define the displacement field components of the frame: $\mathbf{u} = (u_x, u_z)^{\mathrm{T}}$, the fluid displacement relative to the frame: $\mathbf{w} = (w_x, w_z)^{\mathrm{T}}$, the stress tensor components: σ_{ij}, $(i, j = x, z)$, the fluid pressure: p, and the increment of temperature field above the reference absolute temperature T_0,: $T\,(T = T' - T_0)$, where T' is the temperature. The generalized thermo-poroelasticity equations,

including both the LS and GL theories, can be obtained with a modification of the model given in Carcione *et al.* (2019a) as follows,

$$\begin{cases} \sigma_{ij} = 2\mu\epsilon_{ij} + \delta_{ij}(\lambda\epsilon_m + \alpha M\epsilon) - \delta_{ij}\beta(T + \tau_1\dot{T}), \\ -p = M\epsilon - \dfrac{\beta_f}{\phi}(T + \tau_2\dot{T}), \\ \epsilon = \alpha\epsilon_m + \epsilon_f, \epsilon_{ij} = \dfrac{1}{2}(u_{i,j} + u_{j,i}), \\ \epsilon_m = u_{x,x} + u_{z,z}, \epsilon_f = w_{x,x} + w_{z,z}, \end{cases} \tag{1}$$

where δ_{ij} is the Kronecker function, λ and μ are the Lamé constants of the dry rock, ϕ is the porosity, τ_1 and τ_2 are relaxation times representing the dependence of the elastic behaviour on the temperature rate, and β and β_f are coefficients of thermoelasticity of the bulk material and fluid, respectively. The subindex '$,i$' represents a spatial derivative and a dot above a variable denotes a time derivative. Carcione *et al.* (2019a) considered $\tau_1 = \tau_2 = 0$, that is, eq. (1) corresponds to the LS theory. M is related to the elastic coupling between the solid and fluid phases and α is the Biot effective stress coefficient,

$$M = \frac{K_s}{1 - \phi - K_m/K_s + \phi K_s/K_f}, \quad \alpha = 1 - \frac{K_m}{K_s} \tag{2}$$

(Carcione 2014), where $K_m = \lambda + \frac{2}{3}\mu$ is the bulk modulus of the drained matrix, K_s and K_f are the bulk moduli of solid and fluid, respectively.

The equations of momentum conservation are (Carcione *et al.* 2019a)

$$\begin{cases} \sigma_{ij,j} = \rho\ddot{u}_i + \rho_f\ddot{w}_i, \\ -p_{,i} = \rho_f\ddot{u}_i + m\ddot{w}_i + \dfrac{\eta}{\kappa}\dot{w}_i, \end{cases} \tag{3}$$

where $m = \mathcal{T}\rho_f/\phi$, with $\mathcal{T}$ the tortuosity, η is the fluid viscosity, κ is the permeability of the medium, ρ_f is the fluid density, and

$$\rho = (1 - \phi)\rho_s + \phi\rho_f, \tag{4}$$

is the composite density, with ρ_s the solid density.

The Fourier law of heat conduction is (Sharma 2018; Carcione *et al.* 2019a)

$$\gamma\nabla^2 T = c\left(\dot{T} + \tau_3\ddot{T}\right) + T_0\beta\left[(\dot{\epsilon}_m + \tau_4\ddot{\epsilon}_m) + \left(\dot{\epsilon}_f + \tau_4\ddot{\epsilon}_f\right)\right], \tag{5}$$

where γ is the thermal conductivity, c is the specific heat of the unit volume in the absence of deformation, τ_3 and τ_4 are MVC relaxation times, and ∇^2 is the Laplacian operator. In the classical LS theory, $\tau_3 = \tau_4 = \tau$ is assumed (Carcione *et al.* 2019a).

In terms of the displacement vectors $\mathbf{u}$, $\mathbf{w}$ and temperature T, equations (3) can be expressed as

$$\begin{cases} (\lambda + \mu + \alpha^2 M)\nabla\epsilon_m + \mu\nabla^2\mathbf{u} + \alpha M\nabla\epsilon_f - \beta\nabla[T + \tau_1\dot{T}] = \rho\ddot{\mathbf{u}} + \rho_f\ddot{\mathbf{w}}, \\ \alpha M\nabla\epsilon_m + M\nabla\epsilon_f - \dfrac{\beta_f}{\phi}\nabla[T + \tau_2\dot{T}] = \rho_f\ddot{\mathbf{u}} + m\ddot{\mathbf{w}} + \dfrac{\eta}{\kappa}\dot{\mathbf{w}}. \end{cases} \tag{6}$$

Eqs (5) and (6) include both the classic Lord-Shulman (LS) and Green-Lindsay (GL) theories. The former is obtained by using $\tau_1 = \tau_2 = 0$, and $\tau_3 = \tau_4 = \tau$, in which case, the equations become those of Carcione *et al.* (2019a), whereas the second with $\tau_4 = 0$ and $\tau_1 = \tau_2$ (Sharma 2018). Ignaczak & Ostoja-Starzewski (2010, p. 23) show that, in the case of the GL model, the relation $\tau_1 = \tau_2 \geq \tau_3$ holds, and for $\tau_1 = \tau_2 = \tau_3$, the LS and GL theories coincide. In the present work, we also consider a generalization of the classical LS theory by using different values of τ_3 and τ_4.

2.2 Plane-wave analysis

Using the Helmholtz decomposition, the displacement vectors $\mathbf{u}$ and $\mathbf{w}$ can be expressed in terms of two potentials, ϕ and Ψ, as follows:

$$\mathbf{u} = \nabla\phi_s + \nabla\times\Psi_\mathbf{s}, \quad \mathbf{w} = \nabla\phi_f + \nabla\times\Psi_\mathbf{f}, \tag{7}$$

where the subscripts 's' and 'f' refer to the solid and fluid phases, respectively.

Applying the divergence on both sides of eq. (6), we obtain

$$\begin{cases} (\lambda + 2\mu + \alpha^2 M)\nabla^2\epsilon_m + \alpha M\nabla^2\epsilon_f - \beta\nabla^2[T + \tau_1\dot{T}] = \rho\ddot{\epsilon}_m + \rho_f\ddot{\epsilon}_f, \\ \alpha M\nabla^2\epsilon_m + M\nabla^2\epsilon_f - \dfrac{\beta_f}{\phi}\nabla^2[T + \tau_2\dot{T}] = \rho_f\ddot{\epsilon}_m + m\ddot{\epsilon}_f + \dfrac{\eta}{\kappa}\dot{\epsilon}_f. \end{cases} \tag{8}$$

Since $\nabla\cdot\Psi_\mathbf{s} = 0$ and $\nabla\cdot\Psi_\mathbf{f} = 0$, applying the divergence on eq. (7), we have

$$\epsilon_m = \nabla^2\phi_s, \quad \epsilon_f = \nabla^2\phi_f. \tag{9}$$

Substituting eq. (9) into eqs (5) and (8), we obtain the system of equations for the propagation of compressional waves,

$$\begin{cases} (\lambda + 2\mu + \alpha^2 M)\nabla^2\phi_s + \alpha M\nabla^2\phi_f - \beta[T + \tau_1\dot{T}] = \rho\ddot{\phi}_s + \rho_f\ddot{\phi}_f, \\ \alpha M\nabla^2\phi_s + M\nabla^2\phi_f - \dfrac{\beta_f}{\phi}[T + \tau_2\dot{T}] = \rho_f\ddot{\phi}_s + m\ddot{\phi}_f + \dfrac{\eta}{\kappa}\dot{\phi}_f, \\ \gamma\nabla^2 T = c\left(\dot{T} + \tau_3\ddot{T}\right) + T_0\beta\left[\left(\nabla^2\dot{\phi}_s + \tau_4\nabla^2\ddot{\phi}_s\right) + \left(\nabla^2\dot{\phi}_f + \tau_4\nabla^2\ddot{\phi}_f\right)\right]. \end{cases} \tag{10}$$

The plane-wave kernels for the potentials and temperature field are

$$\begin{cases} \phi_s = A_s \exp\left[\mathrm{i}(\mathbf{k_p}\cdot\mathbf{r}-\omega t)\right], \\ \phi_f = A_f \exp\left[\mathrm{i}(\mathbf{k_p}\cdot\mathbf{r}-\omega t)\right], \\ T = A_t \exp\left[\mathrm{i}(\mathbf{k_p}\cdot\mathbf{r}-\omega t)\right], \end{cases} \tag{11}$$

$$\begin{cases} \Psi_{\mathbf{s}} = B_s \exp\left[\mathrm{i}(\mathbf{k_s}\cdot\mathbf{r}-\omega t)\right], \\ \Psi_{\mathbf{f}} = B_f \exp\left[\mathrm{i}(\mathbf{k_s}\cdot\mathbf{r}-\omega t)\right], \end{cases} \tag{12}$$

where A_s, A_f, A_t, B_s and B_f are the amplitudes, ω is the angular frequency, $\mathbf{k_p}$ and $\mathbf{k_s}$ are the wavenumbers of the compressional and shear waves, respectively, and $\mathbf{r}$ is the spatial vector.

Substituting eq. (11) into eq. (10) and after a simplification, we obtain

$$\mathbf{H}\cdot\mathbf{A} = \mathbf{0}, \tag{13}$$

where, $\mathbf{A} = [A_s, A_f, A_t]^{\mathrm{T}}$,

$$\begin{cases} H_{11} = (\lambda + 2\mu + \alpha^2 M)k_p^2 - \rho\omega^2, \\ H_{12} = \alpha M k_p^2 - \rho_f \omega^2, \\ H_{13} = \beta(1 - \mathrm{i}\omega\tau_1), \\ H_{21} = \alpha M k_p^2 - \rho_f \omega^2, \\ H_{22} = M k_p^2 - m\omega^2 - \mathrm{i}\omega\dfrac{\eta}{\kappa}, \\ H_{23} = \dfrac{\beta_f}{\phi}(1 - \mathrm{i}\omega\tau_2), \\ H_{31} = T_0\beta k_p^2(\mathrm{i}\omega + \tau_4\omega^2), \\ H_{32} = T_0\beta k_p^2(\mathrm{i}\omega + \tau_4\omega^2), \\ H_{33} = \gamma k_p^2 - c(\mathrm{i}\omega + \tau_3\omega^2). \end{cases} \tag{14}$$

Non-zero solutions for the compressional waves, are obtained if the determinant of $\mathbf{H}$ is zero, which yields the following dispersion relation,

$$a_6 v_c^6 + a_4 v_c^4 + a_2 v_c^2 + a_0 = 0, \tag{15}$$

where $v_c = \omega/k_p$ is the complex velocity,

$$\begin{aligned} a_0 &= \mathrm{i}\omega^2\phi\gamma ME, \\ a_2 &= \omega\left\{\phi\left[b\gamma E_G - \mathrm{i}\omega\gamma(mE_G + M(\rho - 2\alpha\rho_f)) + cME\bar{\tau}_3\right]\right. \\ &\quad \left.+\beta T_0\bar{\tau}_4\left[\beta_f E\bar{\tau}_2 + (1-\alpha)M(\phi\beta\bar{\tau}_1 - \alpha\beta_f\bar{\tau}_2)\right]\right\}, \\ a_4 &= -b\phi\left[\omega\rho\gamma + \mathrm{i}cE_G\bar{\tau}_3 + \mathrm{i}\beta^2 T_0\bar{\tau}_1\bar{\tau}_4\right] + \omega\left[\mathrm{i}\omega\gamma\phi(m\rho - \rho_f^2) - c\phi\bar{\tau}_3(mE_G\right. \\ &\quad \left.+M(\rho - 2\alpha\rho_f)) - \beta T_0\bar{\tau}_4[\beta\phi(m-\rho_f)\bar{\tau}_1 + \beta_f(\rho - \rho_f)\bar{\tau}_2]\right], \\ a_6 &= c\phi\bar{\tau}_3\left[\mathrm{i}b\rho - \omega(\rho_f^2 - m\rho)\right], \end{aligned} \tag{16}$$

where $E = \lambda + 2\mu$, $E_G = E + \alpha^2 M$, $b = \dfrac{\eta}{\kappa}$, and $\bar{\tau}_l = 1 - \mathrm{i}\omega\tau_l$.

By solving the cubic eq. (15), we obtain three physically meaningful roots v_1, v_2, and v_3, corresponding to the velocities of the fast P (P1), slow P (P2) and T waves, respectively. These velocities, being complex, describe also the attenuation properties. Particularly, if $\beta = \beta_f = 0$, we obtain the velocity for the decoupled thermal wave,

$$v_3 = \sqrt{\frac{\gamma\omega}{\mathrm{i}c\bar{\tau}_3}}. \tag{17}$$

This indicates that the thermal wave is dissipative at low frequencies. On the other hand, the cubic eq. (15) becomes a quadratic one,

$$(\mathrm{i}b\rho + \omega m\rho - \omega\rho_f^2)v_c^4 + (2\omega\alpha M\rho_f - \mathrm{i}bE_G - \omega m E_G - \omega M\rho)v_c^2 + \omega ME = 0, \tag{18}$$

which corresponds to the velocities of the fast and slow P waves.

The potential functions are

$$\begin{cases} \phi_s = \phi_1 + \phi_2 + \phi_3, \\ \phi_f = \nu_1\phi_1 + \nu_2\phi_2 + \nu_3\phi_3, \\ T = \delta_1\phi_1 + \delta_2\phi_2 + \delta_3\phi_3, \end{cases} \tag{19}$$

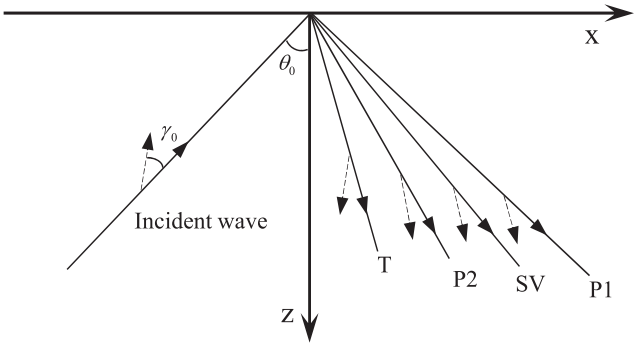

Figure 1. Diagram of the reflection phenomenon at the surface of a generalized thermo-poroelastic medium. The solid and dashed arrows represent the propagation and attenuation directions, respectively.

where the subscripts 1, 2, and 3 represent the fast, slow and *T* waves, respectively. Moreover, v_i and δ_i are related to the ratios A_f/A_s and A_t/A_s, specified with the complex velocity v_i, and can be obtained with the superposition principle by solving eq. (13),

$$\begin{cases} v_i = \dfrac{v_i^2(\rho\beta_f\bar{\tau}_2 - \rho_f\phi\beta\bar{\tau}_1) + \alpha M\phi\beta\bar{\tau}_1 - E_G\beta_f\bar{\tau}_2}{v_i^2(\phi\beta\bar{\tau}_1(m + \dfrac{\mathrm{i}b}{\omega}) - \beta_f\rho_f\bar{\tau}_2) + \alpha M\beta_f\bar{\tau}_2 - \phi M\beta\bar{\tau}_1}, \\ \delta_i = \dfrac{T_0\beta\bar{\tau}_4\omega^2(1+v_i)}{c\bar{\tau}_3 v_i^2 + \mathrm{i}\gamma\omega}. \end{cases} \tag{20}$$

Applying the curl on both sides of eq. (6), we have,

$$\begin{cases} \mu\nabla^2\Psi_{\mathbf{s}} - \rho\ddot{\Psi}_{\mathbf{s}} - \rho_f\ddot{\Psi}_{\mathbf{f}} = 0, \\ \rho_f\ddot{\Psi}_{\mathbf{s}} + m\ddot{\Psi}_{\mathbf{f}} + \dfrac{\eta}{\kappa}\dot{\Psi}_{\mathbf{f}} = 0. \end{cases} \tag{21}$$

Solving eq. (21) with (12), we obtain,

$$\Psi_{\mathbf{f}} = v_4\Psi_{\mathbf{s}},\ \nabla^2\Psi_{\mathbf{s}} = \frac{1}{v_4^2}\ddot{\Psi}_s,\quad v_4 = \sqrt{\frac{\mu}{\rho + \rho_f v_4}},\quad v_4 = -\frac{\rho_f}{m + \mathrm{i}\dfrac{\eta}{\kappa\omega}}, \tag{22}$$

where we use index 4 to represent the shear wave (*SV*-wave). The attenuation of the shear wave is mainly induced by the Biot mechanism and is not affected by the thermal effect.

Following Carcione (2014), the corresponding phase velocities and attenuation factors are given in terms of the complex velocity as,

$$V_i = \left[\mathrm{Re}\left(\frac{1}{v_i}\right)\right]^{-1},\quad Q_i = \frac{\mathrm{Re}(v_i^2)}{\mathrm{Im}(v_i^2)},\quad i = 1, 2, 3, 4, \tag{23}$$

where, "Re" and "Im" represent the real and imaginary parts of a complex variable.

3 REFLECTION AT THE SURFACE

We study the propagation of the reflected waves induced by the incidence of an inhomogeneous wave at the surface of a generalized thermo-poroelastic medium. A half-space occupied by the medium ($z > 0$) with surface defined at $z = 0$ is considered (Fig. 1).

3.1 Potential functions

The medium ($z > 0$) is saturated with viscous fluids and is thermally insulated, thus behaving anelastically. This implies that all the modes (incident and reflected) are attenuated inhomogeneous waves. A general representation of an attenuated wave can be specified by its direction of propagation as well as the direction of maximum attenuation (Carcione 2006, 2014). For an incident *P* wave (denoted with index 0), the potentials and temperature are

$$\begin{cases} \phi_s^{(0)} = A_s^{(0)}\exp\left[\mathrm{i}\omega(p_0x - q_0z) - \mathrm{i}\omega t\right], \\ \phi_f^{(0)} = v_0A_s^{(0)}\exp\left[\mathrm{i}\omega(p_0x - q_0z) - \mathrm{i}\omega t\right], \\ T^{(0)} = \delta_0A_s^{(0)}\exp\left[\mathrm{i}\omega(p_0x - q_0z) - \mathrm{i}\omega t\right], \end{cases} \tag{24}$$

where $A_s^{(0)}$ is the amplitude, p_0 and q_0 are the horizontal and vertical complex slowness, v_0 and δ_0 are the amplitude ratios, determined by eq. (20), with the specific complex velocity v_0 depending on the type of incident wave.

For the *SV*-wave,

$$\begin{cases} \Psi_s^{(0)} = B_s^{(0)} \exp\left[\mathrm{i}\omega(p_0 x - q_0 z) - \mathrm{i}\omega t\right], \\ \Psi_f^{(0)} = \nu_0 B_s^{(0)} \exp\left[\mathrm{i}\omega(p_0 x - q_0 z) - \mathrm{i}\omega t\right], \end{cases} \tag{25}$$

where $B_s^{(0)}$ is the amplitude, ν_0 is the amplitude ratio, equal to ν_4 given in eq. (22).

For a given propagation direction θ_0, the inhomogeneity angle γ_0 (angle between the attenuation and propagation directions, see Fig. 1) and the complex velocity v_0, the horizontal slowness p_0 is defined as (Sharma 2013; Carcione 2014),

$$p_0 = \frac{|\mathbf{P_0}|}{\omega}\sin\theta_0 + \mathrm{i}\frac{|\mathbf{A_0}|}{\omega}\sin(\theta_0 - \gamma_0), \tag{26}$$

with the propagation vector $\mathbf{P_0}$ and the attenuation vector $\mathbf{A_0}$ obtained from

$$\begin{cases} 2|\mathbf{P_0}|^2 = \omega^2\left[\mathrm{Re}(v_0^{-2}) + \sqrt{\left(\mathrm{Re}(v_0^{-2})\right)^2 + \left(\mathrm{Im}(v_0^{-2})/\cos\gamma_0\right)^2}\right], \\ 2|\mathbf{A_0}|^2 = \omega^2\left[-\mathrm{Re}(v_0^{-2}) + \sqrt{\left(\mathrm{Re}(v_0^{-2})\right)^2 + \left(\mathrm{Im}(v_0^{-2})/\cos\gamma_0\right)^2}\right]. \end{cases} \tag{27}$$

The vertical slowness is then

$$q_0 = G_R + \mathrm{i}G_I, \quad G = \pm\mathrm{pv}\sqrt{v_0^{-2} - p_0^2}, \tag{28}$$

where pv represents the principal value of the complex quantity G, and G_R and G_I are the real and imaginary parts of G, respectively. In this way, the negative sign in q_0 ensures the propagation and energy decay of the wave along the negative z-direction.

The incident wave at the surface is reflected as P1, P2, T and SV waves. In the following, these four waves are represented with the indices 1, 2, 3 and 4. The potential functions of the three compressional waves are

$$\begin{cases} \phi_s^{(r)} = \sum_{i=1}^{3}\phi_s^{(i)} = \sum_{i=1}^{3} A_s^{(i)} \exp\left[\mathrm{i}\omega(p_i x + q_i z) - \mathrm{i}\omega t\right], \\ \phi_f^{(r)} = \sum_{i=1}^{3}\phi_f^{(i)} = \sum_{i=1}^{3} \nu_i A_s^{(i)} \exp\left[\mathrm{i}\omega(p_i x + q_i z) - \mathrm{i}\omega t\right], \\ T^{(r)} = \sum_{i=1}^{3} T^{(i)} = \sum_{i=1}^{3} \delta_i A_s^{(i)} \exp\left[\mathrm{i}\omega(p_i x + q_i z) - \mathrm{i}\omega t\right], \end{cases} \tag{29}$$

where p_i and q_i are the horizontal and vertical slowness, respectively. The quantities ν_i and δ_i are the amplitude ratios and can be determined from eq. (20) with the corresponding complex velocity v_i.

The potential function of the reflected shear wave is

$$\begin{cases} \Psi_s^{(r)} = \Psi_s^{(4)} = B_s^{(4)} \exp\left[\mathrm{i}\omega(p_4 x + q_4 z) - \mathrm{i}\omega t\right], \\ \Psi_f^{(r)} = \Psi_f^{(4)} = \nu_4 B_s^{(4)} \exp\left[\mathrm{i}\omega(p_4 x + q_4 z) - \mathrm{i}\omega t\right], \end{cases} \tag{30}$$

where $B_s^{(4)}$ is the amplitude.

Invoking the Snell law (Carcione 2014), the horizontal slowness remains unchanged during the propagation, that is,

$$p_1 = p_2 = p_3 = p_4 = p_0. \tag{31}$$

Then, the vertical slowness can be obtained from the complex velocity v_i as

$$q_i = G_R + \mathrm{i}G_I, G = \pm\mathrm{pv}\sqrt{v_i^{-2} - p_i^2}, \quad i = 1, 2, 3, 4. \tag{32}$$

Positive signs of q_i in eqs (29) and (30) ensure the propagation and decay of the reflected waves along the positive z-direction (Borcherdt 1982).

3.2 Displacements and stresses

Substituting the potential functions into the Helmholtz eq. (7), we obtain the displacements vectors **u** and **w** as

$$\begin{cases} \mathbf{u} = (u_x, u_z)^{\mathrm{T}} = \nabla H_s + \left[-\dfrac{\partial G_s}{\partial z}, \dfrac{\partial G_s}{\partial x}\right]^{\mathrm{T}}, \\ \mathbf{w} = (w_x, w_z)^{\mathrm{T}} = \nabla H_f + \left[-\dfrac{\partial G_f}{\partial z}, \dfrac{\partial G_f}{\partial x}\right]^{\mathrm{T}}, \end{cases} \tag{33}$$

where $H_i = \sigma\phi_i^{(0)} + \phi_i^{(r)}$, $G_i = (1-\sigma)\Psi_i^{(0)} + \Psi_i^{(r)}$, $(i = s, f)$, and $\sigma = 0$ and 1 correspond to the incident P and SV waves, respectively.

The temperature field is then

$$T = \sigma T^{(0)} + T^{(r)}. \tag{34}$$

Using eq. (1), we obtain

$$\begin{aligned}
\sigma_{xx} &= (\lambda + \alpha^2 M)\nabla^2 H_s + \alpha M \nabla^2 H_f + 2\mu \left[\frac{\partial^2 H_s}{\partial^2 x} - \frac{\partial^2 G_s}{\partial x \partial z}\right] - \beta(T + \tau_1 \dot{T}),\\
\sigma_{zz} &= (\lambda + \alpha^2 M)\nabla^2 H_s + \alpha M \nabla^2 H_f + 2\mu \left[\frac{\partial^2 H_s}{\partial^2 z} + \frac{\partial^2 G_s}{\partial x \partial z}\right] - \beta(T + \tau_1 \dot{T}),\\
\sigma_{xz} &= \mu \left[2\frac{\partial^2 H_s}{\partial x \partial z} + \frac{\partial^2 G_s}{\partial^2 x} - \frac{\partial^2 G_s}{\partial^2 z}\right],\\
p &= -\alpha M \nabla^2 H_s - M \nabla^2 H_f + \frac{\beta_f}{\phi}(T + \tau_2 \dot{T}).
\end{aligned} \tag{35}$$

3.3 Reflection coefficients

At the surface ($z = 0$), the normal and tangential stresses σ_{zz} and σ_{xz} are zero. Other conditions specify the type of boundary, that is, impermeable or permeable. For sealed pores (impermeable), no discharge of fluid is allowed, whereas for fully opened pores (permeable), the fluid pressure in the pores vanishes (Sharma 2013). Furthermore, when the surface is thermally insulated, the gradient of T along the z-direction is zero. Hence, the boundary conditions to be satisfied at the surface are

$$\begin{cases}
\sigma_{xz} = 0,\\
\sigma_{zz} = 0,\\
\vartheta w_z - (1 - \vartheta)p = 0,\\
\dfrac{\partial T}{\partial z} = 0,
\end{cases} \tag{36}$$

where $\vartheta = 0$ and 1 defines a permeable and impermeable boundary, respectively.

Combining eqs (33)–(35) with the boundary conditions, we obtain,

$$\mathbf{M} \cdot \mathbf{x} = \mathbf{y}, \tag{37}$$

where $\mathbf{x}$ is the amplitude vector, defined by $\mathbf{x} = [A_s^{(1)}, A_s^{(2)}, A_s^{(3)}, B_s^{(4)}]^{\mathrm{T}}$. The expressions of the elements of $\mathbf{M}$ and $\mathbf{y}$ are given in Appendix A.

Solving eq. (37) ($\sigma = 1$ and 0 for the P and SV waves, respectively), we obtain the amplitude ratio

$$X_i = \begin{cases} x_i / A_s^{(0)}, & \sigma = 1,\\ x_i / B_s^{(0)}, & \sigma = 0, \end{cases} \tag{38}$$

where x_i is the component of vector $\mathbf{x}$. X_i can then be converted to the reflection coefficient as

$$R_i = X_i \frac{k_i}{k_0} = |R_i| e^{\mathrm{i}\theta_i}, \quad i = 1, 2, 3, 4, \tag{39}$$

where k_i and k_0 are the wavenumbers of the reflected and incident waves, respectively. $|R_i|$ is the reflection amplitude and the θ_i defines the phase angle.

4 ENERGY PARTITIONS

Across a surface element of unit area, the scalar product of the surface traction and the particle velocity represents the energy flux E. The time average of E over a period, denoted by $\langle E \rangle$, is the average energy intensity. Following Singh (2007) and Sharma (2013), the time average of the product of real parts of the two complex functions f and F having forms as eqs (11) and (12) satisfies

$$\langle \mathrm{Re}(F) \cdot \mathrm{Re}(f) \rangle = \frac{1}{2}\mathrm{Re}(F f'), \tag{40}$$

where $\langle \cdot \rangle$ represents a temporal average over a period and the apostrophe is the complex conjugate. Therefore, at the interface, with a normal along the z-direction, the averaged energy intensity of a wave in thermo-poroelastic media is (Sharma 2018)

$$\langle E \rangle = \frac{1}{2}\mathrm{Re}(\sigma_{zz} \dot{u}_z' + \sigma_{xz} \dot{u}_x' - p \dot{w}_z'). \tag{41}$$

The energy intensity is computed with the stress and particle-velocity components associated with the incident and four reflected waves. Therefore, the energy partitions can be obtained by solving a matrix system of order five as follows:

$$\langle \mathbf{E} \rangle = \langle E_{ij} \rangle = \frac{1}{2}\mathrm{Re}(\mathbf{C}_{5\times 3} \cdot \dot{\mathbf{D}}'_{3\times 5}), \quad i, j = 0, 1, 2, 3, 4, \tag{42}$$

Table 1. Medium properties.

Grain bulk modulus, K_s	35 GPa
Density, ρ_s	2650 kg m^{-3}
Frame bulk modulus, K_m	1.7 GPa
Shear modulus, μ	1.885 GPa
Porosity, ϕ	0.3
Permeability, κ	1 darcy
Tortuosity, $\mathcal{T}$	2
Water density, ρ_f	1000 kg m^{-3}
Viscosity, η	0.001 Pa s
Bulk modulus, K_f	2.4 GPa
Thermoelasticity coefficient, β_f	0.8 $\times 10^6$ kg m^{-1} s^{-2} $^\circ$K^{-1}
Bulk specific heat, c	1.8 $\times 10^6$ kg m^{-1} s^{-2} $^\circ$K^{-1}
Thermoelasticity coefficient, β	2.4 $\times 10^6$ kg m^{-1} s^{-2} $^\circ$K^{-1}
Absolute temperature T_0	300 $^\circ$K
Thermal conductivity, γ	4.5 m kg s^{-3} $^\circ$K^{-1}
Relaxation time, τ_1	0.3 ns
‘’ , τ_2	0.3 ns
‘’ , τ_3	0.15 ns
‘’ , τ_4	0.15 ns

where

$$\mathbf{C}_{5\times 3} = \begin{pmatrix} \sigma_{zz}^{(0)} & \sigma_{xz}^{(0)} & -p^{(0)} \\ \sigma_{zz}^{(1)} & \sigma_{xz}^{(1)} & -p^{(1)} \\ \sigma_{zz}^{(2)} & \sigma_{xz}^{(2)} & -p^{(2)} \\ \sigma_{zz}^{(3)} & \sigma_{xz}^{(3)} & -p^{(3)} \\ \sigma_{zz}^{(4)} & \sigma_{xz}^{(4)} & -p^{(4)} \end{pmatrix}, \quad \mathbf{D}_{3\times 5} = \begin{pmatrix} u_z^{(0)} & u_z^{(1)} & u_z^{(2)} & u_z^{(3)} & u_z^{(4)} \\ u_x^{(0)} & u_x^{(1)} & u_x^{(2)} & u_x^{(3)} & u_x^{(4)} \\ w_z^{(0)} & w_z^{(1)} & w_z^{(2)} & w_z^{(3)} & w_z^{(4)} \end{pmatrix}. \tag{43}$$

The diagonal entries $\langle E_{ii}\rangle$ identify the energy fluxes of the incident wave, and the reflected P1, P2, T and SV waves, whereas the off-diagonal entries are the interference energy fluxes. The energy fluxes are scaled to that of the incident wave $\langle E_{00}\rangle$ to obtain the energy ratios as

$$ER_{ij} = \langle E_{ij}\rangle / \langle E_{00}\rangle, \quad i, j = 0, 1, 2, 3, 4. \tag{44}$$

The interference energy ratio of the incident wave with the four reflected waves is

$$ER_{ir} = \sum_{i=1}^{4} (ER_{i0} + ER_{0i}). \tag{45}$$

Similarly, the corresponding interference energy ratio among the four reflected waves is

$$ER_{rr} = \sum_{i=1}^{4} \left(\sum_{j=1}^{4} ER_{ij} - ER_{ii} \right). \tag{46}$$

With the above definitions, the energy conservation at the surface is guaranteed, that is,

$$ER_{\text{cons}} = \sum_{i=1}^{4} ER_{ii} + ER_{ir} + ER_{rr} = -1. \tag{47}$$

5 EXAMPLES

We consider the properties given in Table 1, taken from Carcione *et al.* (2019a) except for the thermoelasticity properties β_f, β, c, γ and relaxation times. The relation $\Gamma = \beta/c$ defines the dimensionless Grüneisen ratio and is equal to 1.33, corresponding to a rock (Anderson 2000).

Fig. 2 shows the variations in phase velocities and dissipation factors as a function of frequency. The fast P1 wave has two relaxation peaks at approximately 10 kHz and 1 GHz. The former is caused by the Biot mechanism and induces velocity dispersion of the P1 and P2 waves. The later one is caused by the thermal effect, which only affects propagation at high frequencies. In comparison with the LS theory, the GL model predicts a higher P1-wave thermal attenuation, and consequently a more pronounced velocity dispersion. The P2 and T waves are dissipative at low frequencies and wavelike at high frequencies. Beyond the thermal relaxation frequency, the GL theory gives a higher P2-wave velocity than that of the LS model, whereas the opposite behaviour is observed for the velocity of the T wave. Compared with the classical Biot theory, the thermoelasticity equations predict a higher velocity of the fast P1 wave for all frequencies and a faster propagation of the slow P2 wave at high frequencies. It is evident that the thermal effects affect the wave propagation and consequently the reflection at the surface. In the following, to highlight the thermal effect as well as the differences between LS and GL models, we consider an incident wave with a frequency of 1 GHz that corresponds to the thermal relaxation peak.

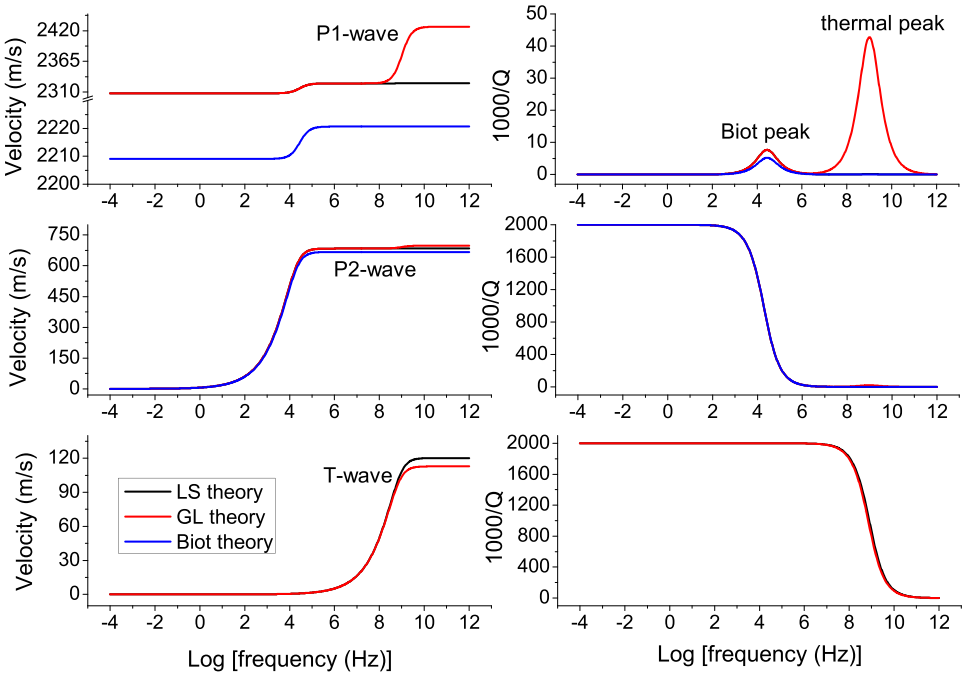

Figure 2. Phase velocities and dissipation factors of the three compressional waves as a function of frequency. The red, black and blue lines correspond to the results of the GL theory, LS theory and the Biot theory, respectively.

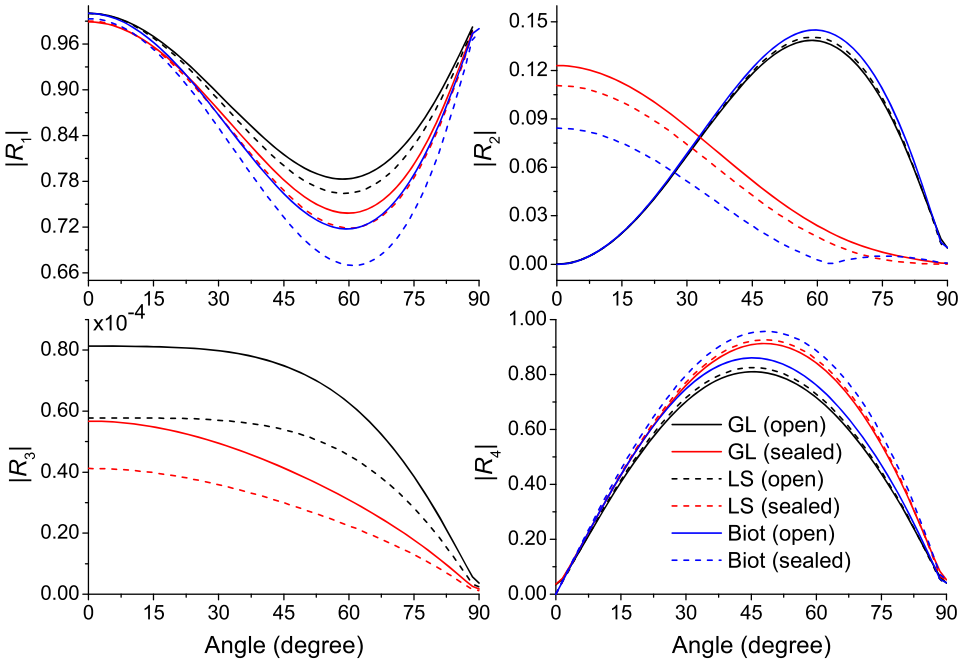

Figure 3. Reflection amplitudes as a function of the incidence angle (incident P1 wave). The red and black lines correspond to sealed and open boundaries, whereas the dashed and solid lines to the results of LS and GL theories, respectively. The blue lines correspond to results of the Biot theory. The subindices 1, 2, 3 and 4 refer to the fast *P*, slow *P*, *T* and *S* waves, respectively.

5.1 P1-wave incidence

Figs 3 and 4 show the reflected amplitudes and phases, respectively, as a function of the incidence angle in the case of an incident P1 wave with a 1 GHz frequency and $\gamma_0 = 45^\circ$. With the same boundary (open or sealed), the GL theory predicts higher amplitudes of the reflected P1 wave than the LS theory, and a slightly weaker reflected *SV*-wave amplitude, whereas the classical Biot theory predicts the opposite effect. At normal incidence, no shear wave is reflected, and the magnitude of the reflected P1 wave is almost 1, whereas the phase difference with respect to the incidence wave is π, indicating that the phenomenon of half-wave loss occurs, as in the case of reflection from the surface of an elastic

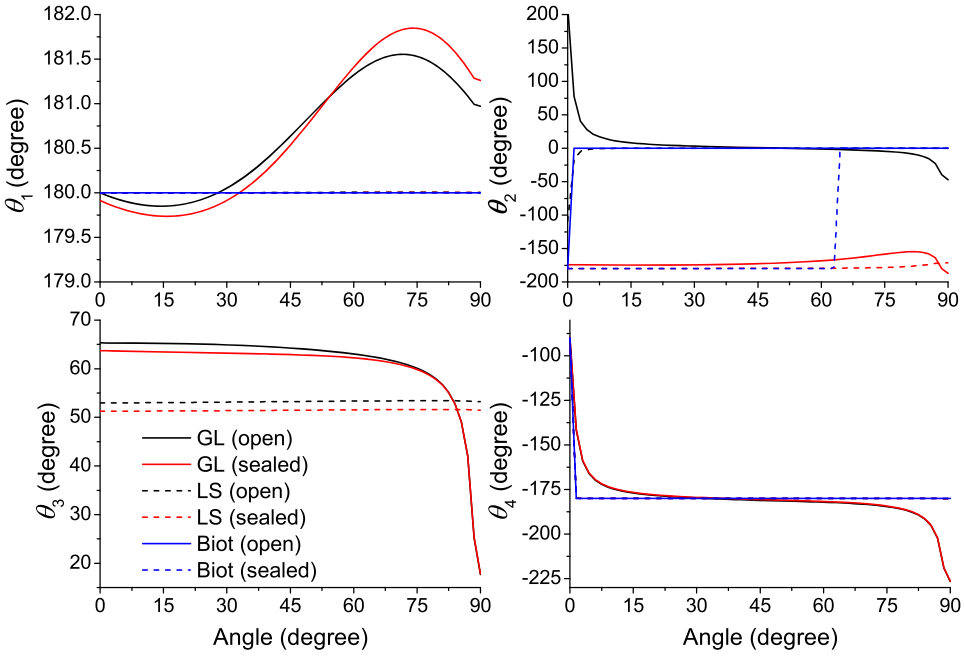

Figure 4. Phases as a function of the incidence angle (incident P1 wave), corresponding to Fig. 3.

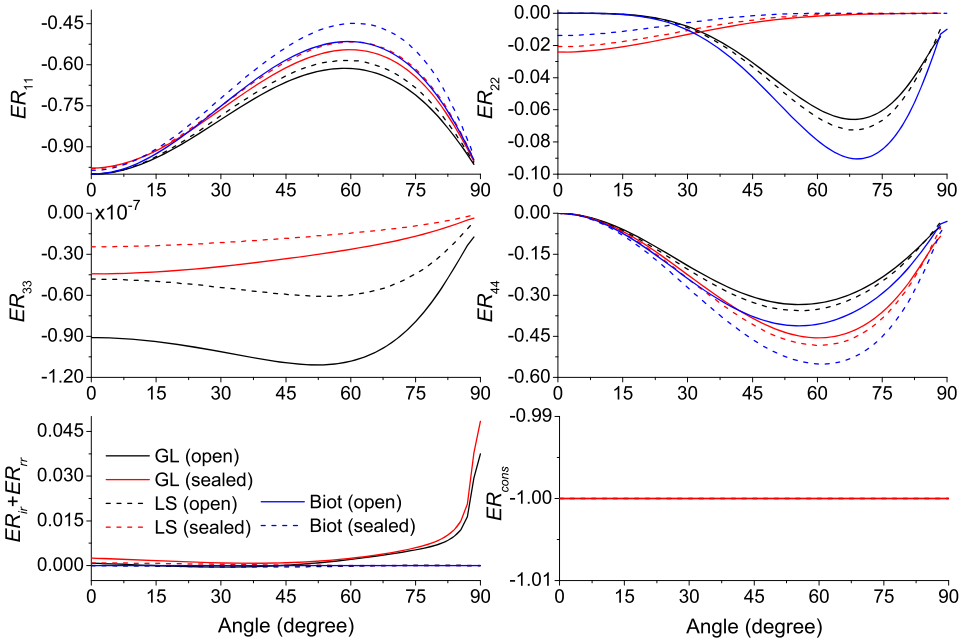

Figure 5. Energy partitions as a function of the incidence angle (incident P1 wave), corresponding to Fig. 3.

solid. The deviation of the P1-wave magnitude from 1 at normal incidence is due to the conversion to slow *P* and *T* waves. The boundary conditions at the interface affect the reflection behaviour. Compared to the sealed boundary, the open boundary yields higher amplitudes of the reflected P1 and *T* waves, but lower amplitude of the reflected *SV* wave. The Biot theory yields the smallest P2-wave magnitudes when the surface is sealed and the opposite response at large incidences is observed when the surface is open. The GL model predicts continuous *P*-wave and *SV*-wave phase variations with incidence angle, unlike the Biot and LS models.

Fig. 5 shows the energy partitions, where the main energy is shared by the P1 and *SV* waves. The P1-wave energy decays (in absolute value) as the angle increases from normal incidence. After a minimum at nearly 60°, the energy increases until grazing incidence. In agreement with the amplitudes, the GL model has a higher P1-wave absolute energy ratio than the LS theory, whereas the Biot theory predicts the smallest value. The open boundary strengthens the energy in comparison with the sealed surface. The opposite behaviour is observed for the reflected *SV* wave, which indicates energy conversion at the surface.

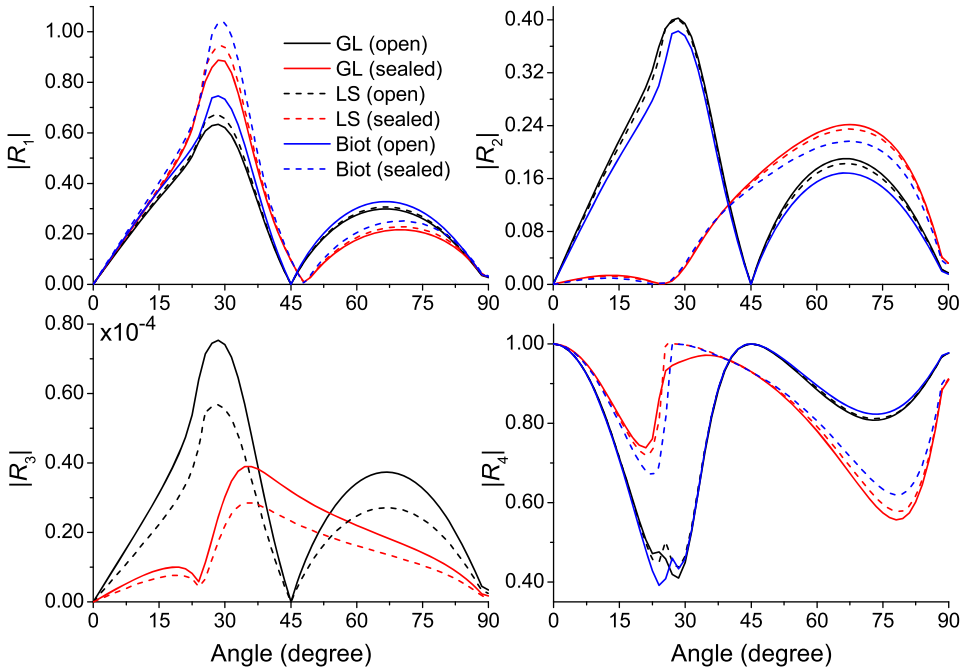

Figure 6. Reflection amplitudes as a function of the incidence angle (incident *SV* wave). The red and black lines correspond to sealed and open boundaries, whereas the dashed and solid lines to the LS and GL theories, respectively. The blue lines correspond to results of the Biot theory. The subindices 1, 2, 3 and 4 refer to the fast *P*, slow *P*, *T* and *S* waves, respectively.

Near normal incidence, the GL model predicts a higher P2-wave energy ratio than the LS one, whereas the Biot theory exhibits the smallest value in the case of a sealed boundary. The behaviour is opposite at high incidence angles when the boundary is open. The *T* wave exhibits a much weaker energy, with the GL theory predicting more energy than the LS one, and the open boundary induces more energy, in agreement with the *T*-wave amplitude. The interference energy corresponding to the GL theory is high near grazing incidence, indicating that more energy conversion occurs. The LS theory predicts almost zero interference energy for all incidence angles as the classical Biot theory, due to the negligible thermal attenuation. The sum of all the ratios is -1, which implies the energy conservation at the surface.

5.2 *SV*-wave incidence

Next, an incident *SV* wave is considered. Figs 6 and 7 show the reflection amplitudes and phase versus incidence angle, and Fig. 8 shows the energy partitions, respectively. The reflection differences are mainly significant at the peaks and minima. The GL model predicts a lower P1-wave amplitude than the LS one, whereas the classical Biot theory exhibits the highest value. Compared with the open boundary, the sealed one predicts higher P1- and *SV*-wave amplitudes near the first maximum and a lower P2-wave amplitude. The opposite behaviour is observed at the second maximum. The GL model yields increased *T*-wave amplitude than the LS one. The significant thermal attenuation of the GL model induces quite different *SV*-wave phases compared to those of the LS and Biot models for both boundaries.

Because the *SV* wave has a lower velocity than the P1 wave, there exists a critical angle. The LS theory predicts a very low attenuation (see Fig. 2) and the medium behaves elastic at 1 GHz. In this case, for incidences beyond the critical angle, the reflected P1 wave propagates along the interface and carries no energy vertically. ER_{11} then becomes zero (dashed lines in Fig. 8). A critical angle at around 25° can be seen. On the other hand, the GL theory predicts significant attenuation and hence the P1 wave is still reflected back into the medium due to the dissipation. In fact, beyond 25° the reflected P1 wave carries energy vertically, decreasing gradually towards grazing incidence. The energy of reflected *SV* wave is affected correspondingly, with an energy-ratio increasing to 1 (in absolute value) in the case of the LS theory (the red dashed line). The same phenomenon has been illustrated by Sharma (2013), who studied the reflection of inhomogeneous waves at the surface of a double-porosity medium.

The LS model predicts a higher P1-wave energy peak than the GL theory, and the sealed boundary further contributes. The P2 wave exhibits the same order of amplitudes of the P1 and *SV* waves. As above, the *T* wave has a very low energy. The GL model predicts more interference energy than the LS one for both, open and sealed boundaries, which implies that more significant energy conversion occurs. The sealed boundary predicts a negative interference energy, but the conservation at the interface is satisfied. A similar phenomenon was observed at the surface of a double-porosity medium (Sharma 2013). As a contrast, the Biot theory gives no interference energy for all incidences.

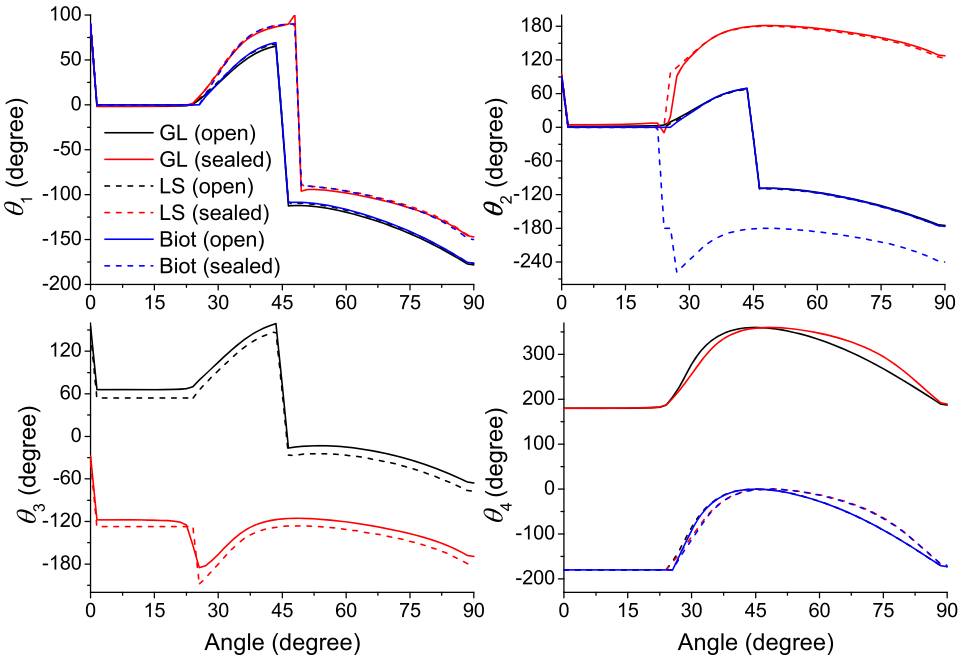

Figure 7. Phases as a function of the incidence angle (incident *SV* wave),corresponding to Fig. 6.

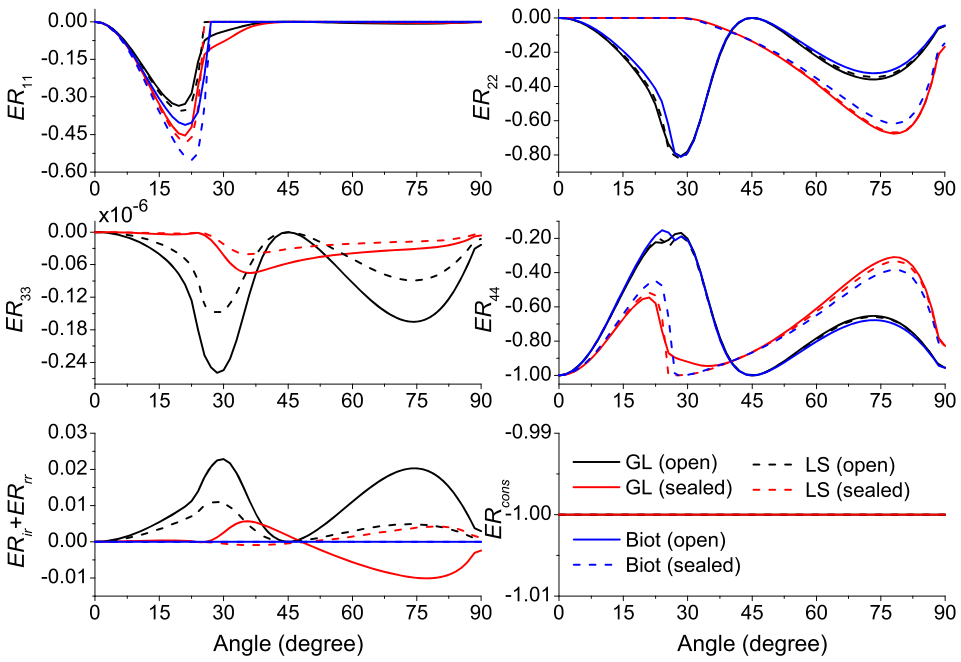

Figure 8. Energy partitions as a function of the incidence angle (incident *SV* wave), corresponding to Fig. 6.

5.3 Generalized LS theory

The classical LS theory assumes $\tau_3 = \tau_4 = \tau$. In this section, we generalize this theory by assuming different values of these relaxation times. Numerical analysis shows that $\tau_4 < \tau_3$ predicts negative attenuation, and therefore wave propagation is unstable. As a contrast, if $\tau_4 \geq \tau_3$, the propagation is stable and can be used to generalize the LS theory.

Fig. 9 shows the phase velocities and dissipation factors of the three compressional waves as a function of frequency, with three different values of τ_4. We observe that increasing τ_4 implies a higher P1-wave thermal attenuation, and consequently more velocity dispersion, while the relaxation frequency remains unchanged. Correspondingly, the P2- and *T*-wave velocities increase and decrease at high frequencies, respectively. Particularly, for $\tau_4 = 0.3$ ns, the phase velocity and dissipation factor are in good agreement with those of the GL model given in Fig. 2. It is clear that by varying τ_4, we can obtain different levels of attenuation.

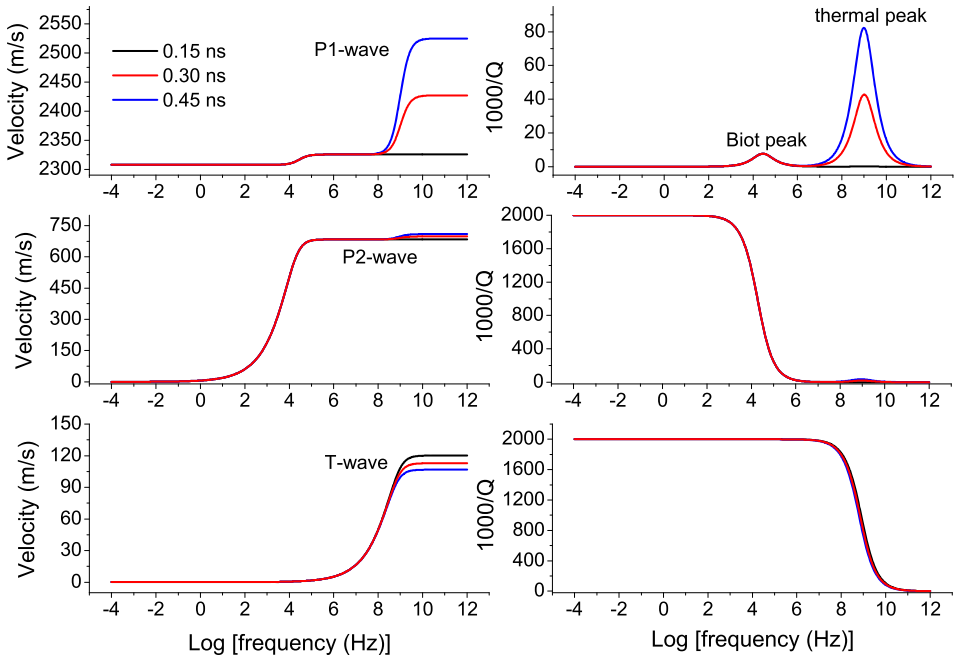

Figure 9. Phase velocities and dissipation factors of the three compressional waves as a function of frequency for the generalized LS theory with different values of τ_4.

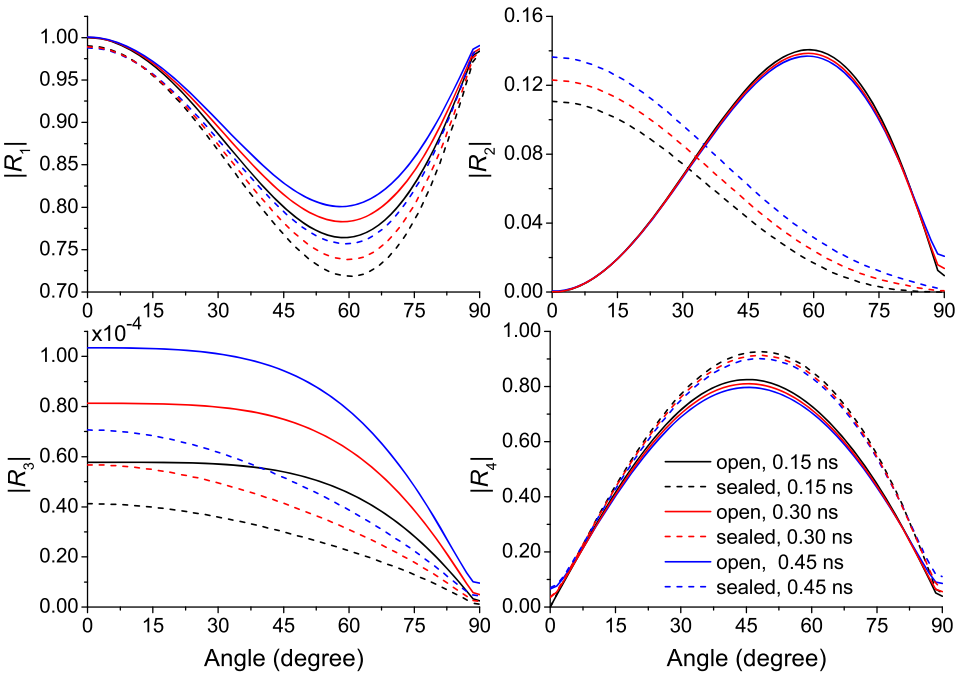

Figure 10. Reflection amplitudes as a function of the incidence angle (incident P1 wave) for the generalized LS theory with different values of τ_4. The dashed and solid lines correspond to sealed and open boundaries, respectively. The subindices 1, 2, 3 and 4 refer to the fast *P*, slow *P*, *T* and *S* waves, respectively.

Figs 10 and 11 show the reflection amplitudes and energy ratios versus incidence angle in the case of an incident P1 wave. Increasing τ_4 increases the P1 and *T* amplitudes, irrespective if the surface is open or sealed. The opposite behaviour is noted for the reflected *SV* wave. The energy ratios show similar variations. The interference energy near the grazing incidence is significantly strengthened as τ_4 increases for both the sealed and open boundaries, showing a similar behaviour of the GL model. Note that for $\tau_3 = \tau_4 = 0.15$ ns, the interference energy is negligible for all incidence angles.

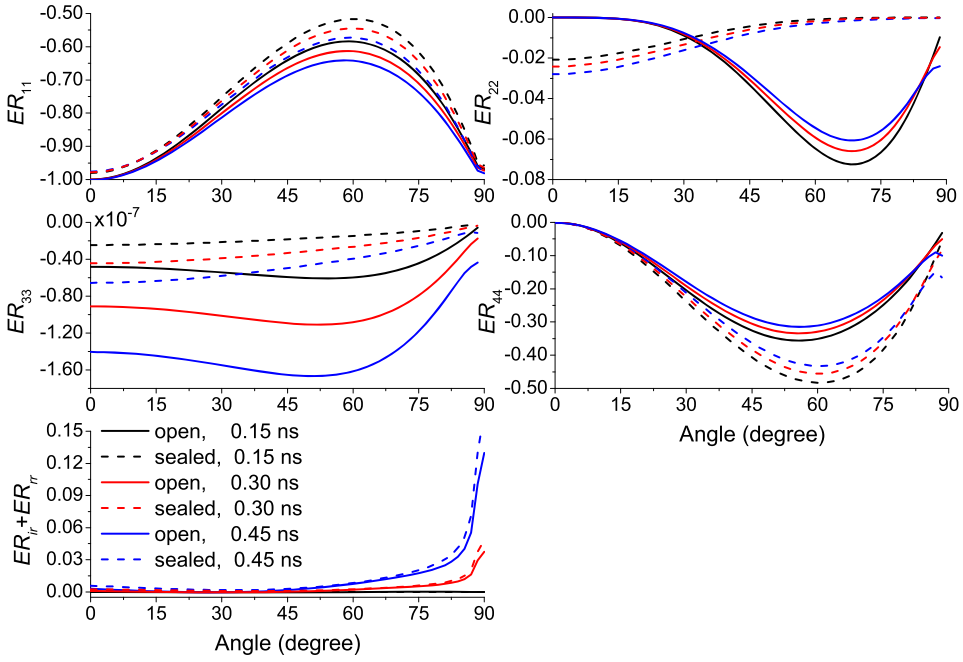

Figure 11. Energy partitions as a function of the incidence angle (incident P1 wave) for the generalized LS theory with different values of τ_4. The dashed and solid lines correspond to sealed and open boundaries, respectively. The subindices 1, 2, 3 and 4 refer to the fast *P*, slow *P*, *T* and *S* waves, respectively.

6 DISCUSSION

6.1 Effect of the inhomogeneity angle

The inhomogeneity angle $\gamma_0 \in (-\pi/2, \pi/2)$ is the angle between the attenuation and propagation directions, as illustrated in Fig. 1. In the case of incident P1 wave, as shown in Fig. 2, the LS theory predicts a negligible thermal attenuation, which implies that $\mathrm{Re}(v_0^2)/\mathrm{Im}(v_0^2) \approx \infty$. This leads to the following approximations:

$$\begin{cases} 2|\mathbf{P_0}|^2 = \omega^2 \mathrm{Re}(v_0^{-2}) \left[1 + \sqrt{1 + \left(\dfrac{\mathrm{Im}(v_0^{-2})}{\mathrm{Re}(v_0^{-2})\cos\gamma_0}\right)^2}\right] \approx 2\omega^2 \mathrm{Re}(v_0^{-2}), \\ 2|\mathbf{A_0}|^2 = \omega^2 \mathrm{Re}(v_0^{-2}) \left[-1 + \sqrt{1 + \left(\dfrac{\mathrm{Im}(v_0^{-2})}{\mathrm{Re}(v_0^{-2})\cos\gamma_0}\right)^2}\right] \approx 0. \end{cases} \tag{48}$$

In this case, the horizontal wavenumber p_0 becomes real and independent of γ_0. The reflection amplitudes obtained with the LS theory for open and sealed boundaries further validate this. In contrast, the GL model yields a non-negligible thermal attenuation and the attenuation vector $\mathbf{A_0}$ in eq. (48) becomes significant, particularly when γ_0 is relative high (close to $\pm 90^\circ$). Thus, the reflection behaviour depends on γ_0.

Fig. 12 shows the reflection amplitudes versus incidence angle for sealed and open boundaries and five different inhomogeneity angles. When $\gamma_0 = 0^\circ$, the incident wave is homogeneous. Note that the three results, with $\gamma_0 = 0^\circ, -40^\circ$ and $+40^\circ$, overlap. This implies that at relatively low γ_0, the reflection amplitudes are similar. The main reason is that the variation in $\mathrm{Im}(v_0^{-2})/\left[\mathrm{Re}(v_0^{-2})\cos\gamma_0\right]$ in eq. (48) is very small. However, this term contributes for high γ_0. For example, for γ_0 equal to 0° , 45° and 80°, this term is 0.04, 0.06 and 0.25, respectively, which in turn implies a significantly increased attenuation factor $\mathbf{A_0}$, and consequently a substantial deviation from the reflection behaviour at $\gamma_0 = 0^\circ$. With a high γ_0 (in absolute value, $+80^\circ$or -80°), the P1-wave amplitude close to the normal incidence increases. The opposite behaviour is observed at the peak, with $+80^\circ$giving a more significant decrease than -80°.

The influence of γ_0 on the *SV* wave is significant for almost all incidence angles. In the case of high γ_0 (in absolute value, $+80^\circ$or -80°), the *SV*-wave amplitude increases. The effect is most evident at normal and grazing incidences. Particularly, the *SV*-wave amplitude at normal incidence becomes non-zero, which is quite different from the behaviour for a low γ_0. The main reason is due to the high attenuation induced by the high inhomogeneity angle. The influence on the *T* wave is only important at angles close to the grazing incidence, where a high absolute value of γ_0 causes a higher amplitude. The effect on the P2-wave amplitude is only important when the surface is open and the inhomogeneity angle is high, say 80° in absolute value. The influence of γ_0 on the energy partitions is significant, as shown in Fig. 13, particularly at angles close to grazing incidence. At these angles, a high γ_0 causes increased energy ratios of the reflected P2, *T* and *SV* waves, and consequently more interference energy, implying that more energy conversion occurs.

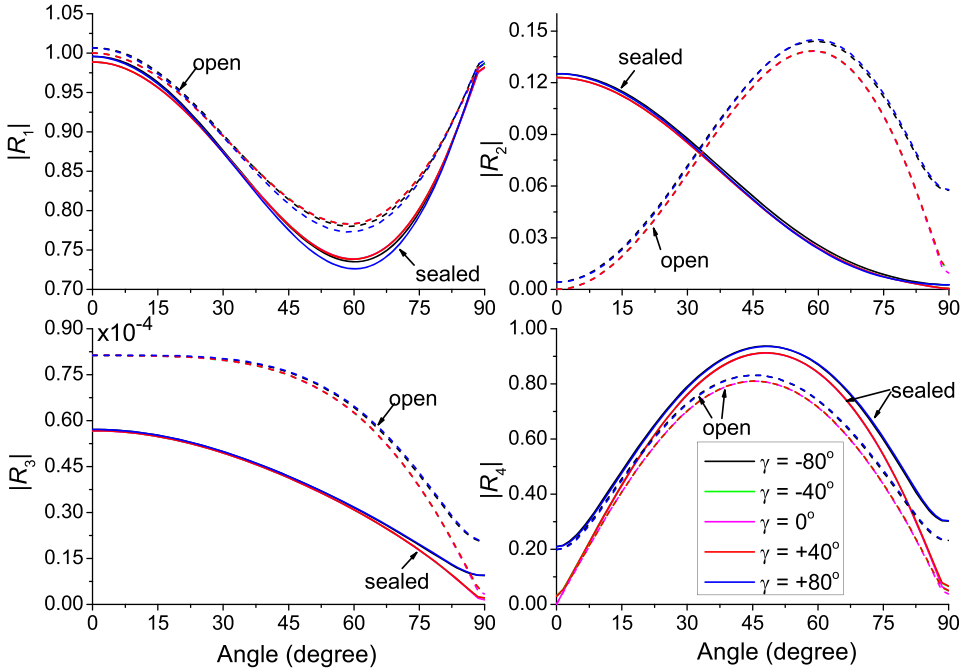

Figure 12. Reflection amplitudes as a function of the incidence angle (incident P1 wave) for the GL theory with different values of γ_0. The dashed and solid lines correspond to open and sealed boundaries, respectively. The subindices 1, 2, 3 and 4 refer to the fast *P*, slow *P*, *T* and *S* waves, respectively.

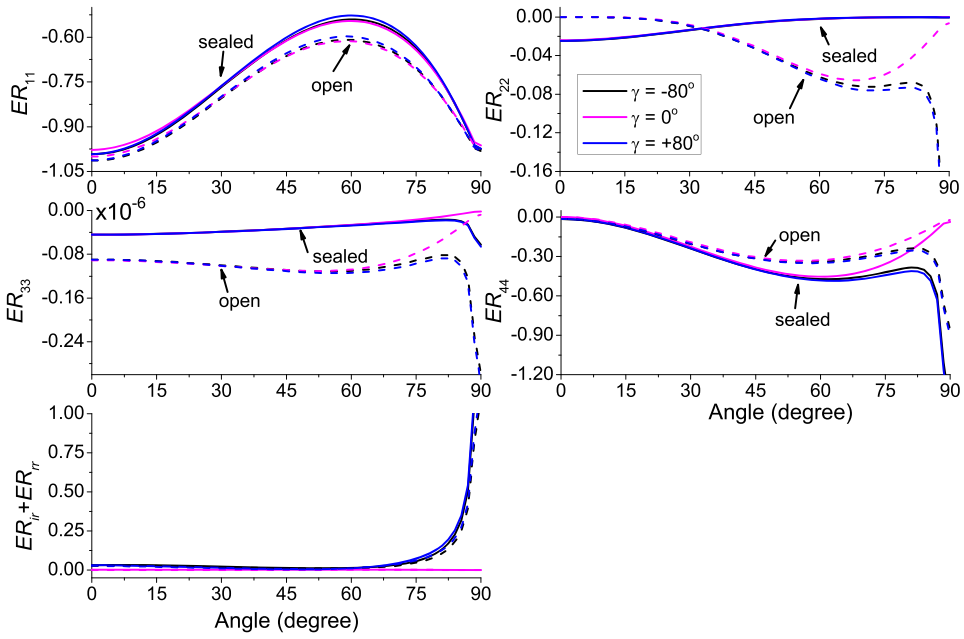

Figure 13. Energy partitions as a function of the incidence angle (incident P1 wave) for the GL theory with different values of γ_0. The dashed and solid lines correspond to open and sealed boundaries, respectively. The subindices 1, 2, 3 and 4 refer to the fast *P*, slow *P*, *T* and *S* waves, respectively.

Liu *et al.* (2020b) studied the reflection at the surface of an effective Biot solid, where they expressed the plane wave using the inhomogeneity parameter D instead of γ_0. The relation between D and γ_0 is

$$\cos\gamma_0 = \frac{\pm 1}{\sqrt{1 + \dfrac{D^2}{[\mathrm{Im}(v_0^{-1})]^2}}}. \tag{49}$$

It is evident that γ_0 increases with D. Particularly, if $D = \infty$, γ_0 becomes $\pm 90^\circ$. Liu *et al.* (2020b) obtained significant P2- and *SV*-wave energies and also more interference energy near grazing incidence, when using a high D. This is consistent with our results.

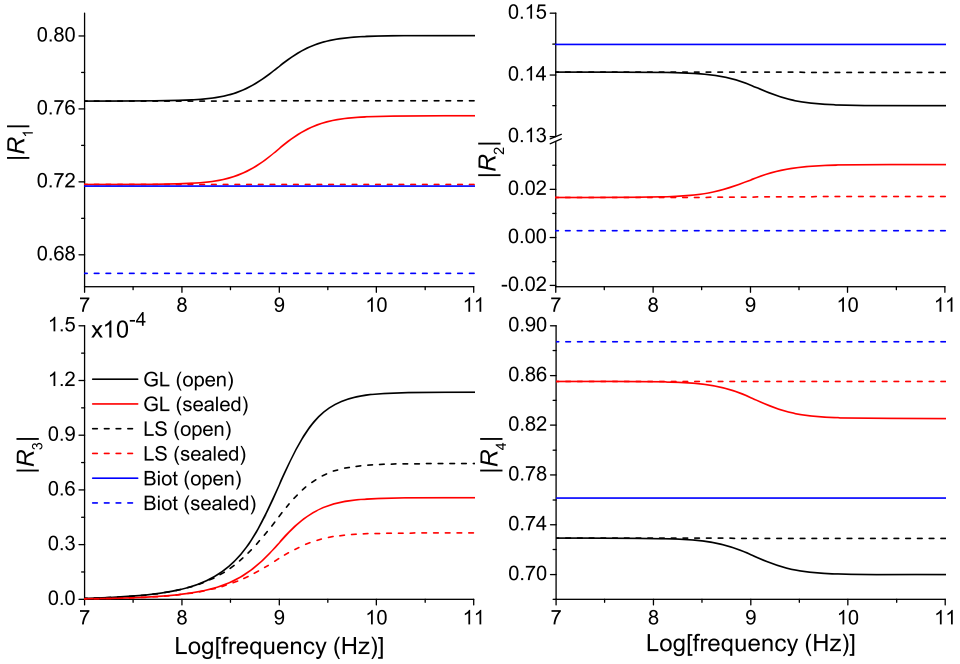

Figure 14. Reflection amplitudes as a function of frequency with a 60° incidence angle (incident P1 wave). The black and red lines correspond to open and sealed boundaries, whereas the solid and dashed lines to the GL and LS models, respectively. The blue lines correspond to results of the Biot theory. The subindices 1, 2, 3 and 4 refer to the fast *P*, slow *P*, *T* and *S* waves, respectively.

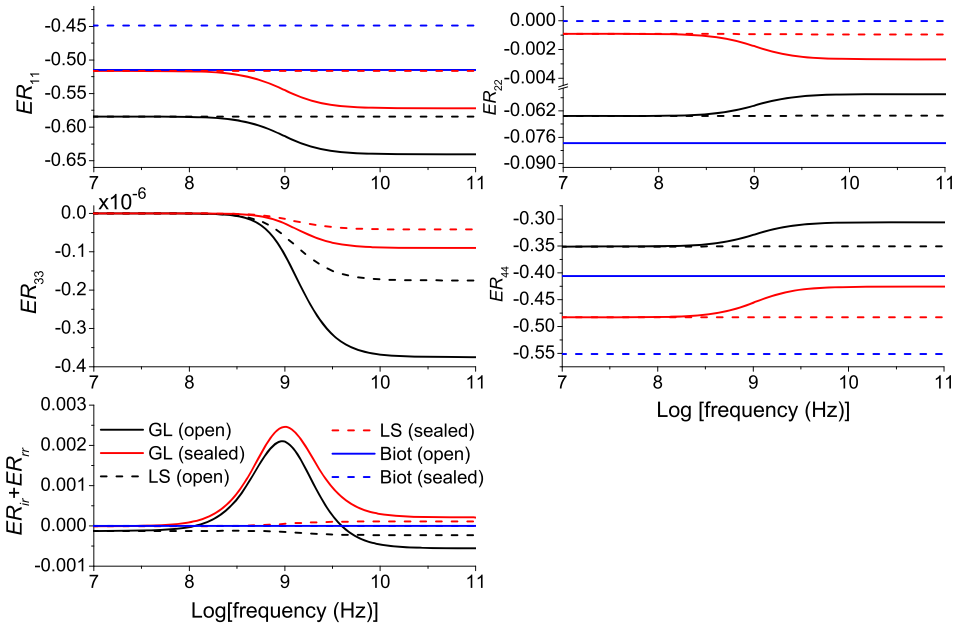

Figure 15. Reflection energy partitions as a function of frequency, corresponding to Fig. 14. The subindices 1, 2, 3 and 4 refer to the fast *P*, slow *P*, *T* and *S* waves, respectively.

The incident *SV* wave is not attenuated by the thermal effect at high frequencies, and hence the reflections at the surface remain unaffected by the inhomogeneity angle, as in the case of P1-wave incidence based on the LS model.

6.2 Effect of frequency

The frequency-dependent velocities given in Fig. 2 imply that the reflections at the surface are frequency-dependent. As an example, we show the case of an incident P1 wave. Figs 14 and 15 show the reflection amplitudes and energy ratios as a function of frequency for $\theta_0 = 60^\circ$ and $\gamma_0 = 45^\circ$. The GL model predicts frequency-dependent P1-, P2- and *SV*-wave amplitudes and energy ratios, irrespective if the surface is open

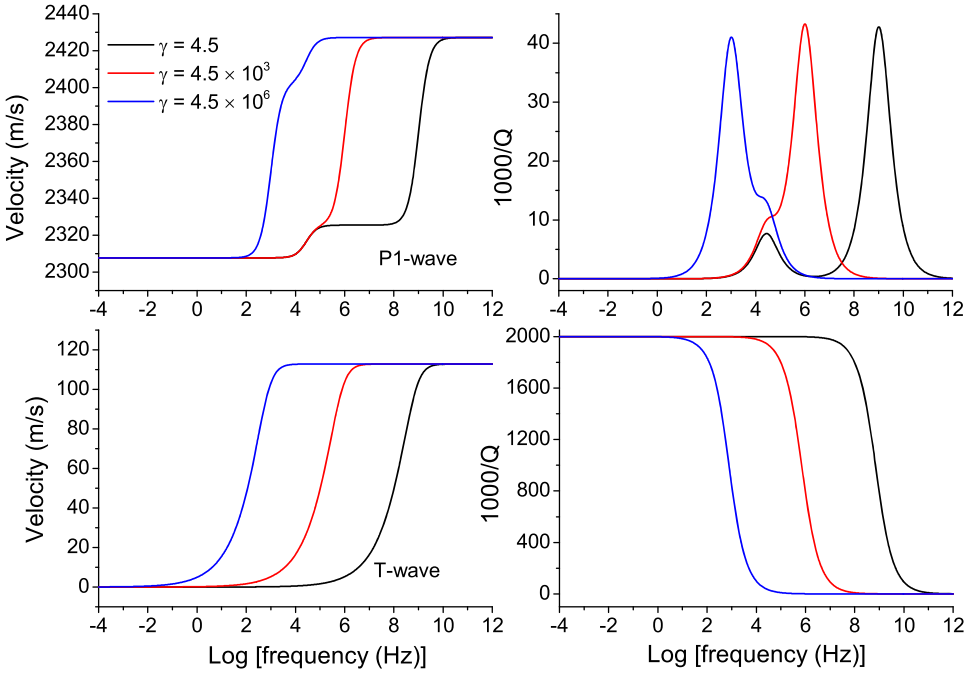

Figure 16. Phase velocities and dissipation factors of the P1 and *T* waves as a function of frequency calculated with the GL model. The black lines correspond to the GL model with γ and τ_i ($i = 1,2,3$) given in Table 1, whereas the blue and red lines to results with γ and τ_i multiplied by 10^3 and 10^6, respectively.

or sealed, whereas the LS and Biot models do not. On the frequency band [0.1, 10] GHz and for both boundaries, the amplitudes and energies of the P1 and *T* wave increase, whereas those of the *SV* wave decrease, compared to the results of the LS model. As a consequence, the interference energy is enhanced. Note that the interference energy predicted by the LS model is close to zero for almost all frequencies. The Biot theory exhibits different amplitudes and energy partitions for the two boundaries, since the P1-wave propagation velocity is different. Its interference energy is zero at all frequencies.

The reflection dispersion is mainly induced by the thermal attenuation. With increasing τ_4 (higher than τ_3), the generalized LS model predicts a higher thermal attenuation, which induces reflection dispersion as the GL model. According to Carcione *et al.* (2019b), the thermal relaxation frequency depends on the values of γ and τ_i. In the classical LS thermoelasticity theory ($\tau = \tau_3 = \tau_4$), the thermal relaxation peak location is

$$f_p \approx \frac{1}{2\pi\tau}, \tag{50}$$

where $\tau = \gamma/(cv^2)$, with $v = \sqrt{(\lambda + 2\mu)/\rho}$ the isothermal phase velocity. Thus, increasing γ (or τ), the peak moves to low frequencies. Fig. 16 shows that increasing γ (or equivalently τ_i) also moves the thermal relaxation peak of the GL model to the low frequencies. In real applications, γ ranges from 24000 m kg s^{-3} °K^{-1} for CRC aluminium to 0.023 m kg s^{-3} °K^{-1} for air, whereas rocks filled with fluids have a range between 1 and 12 m kg s^{-3} °K^{-1}. Carcione *et al.* (2019b) obtained a relaxation peak at seismic frequencies with $\gamma = 4.5 \times 10^6$ m kg s^{-3} °K^{-1}, for a better illustration of the physics. If a similar γ is used here, the reflection dispersion is significant at low frequencies.

7 CONCLUSIONS

We consider a unified thermo-poroelasticity theory, including the GL and LS models and a generalized LS model, to compute the reflection coefficient of an incident inhomogeneous plane wave on a thermally insulated surface. The results show that the GL model predicts a significantly higher P1-wave thermal attenuation than the classical LS model and consequently induces more interference energy, implying that more energy conversion occurs. The generalized LS model predicts enhanced P1-wave thermal attenuation with increasing MVC relaxation time, and gives more interference energy, similar to the GL model. In the presence of strong thermal attenuation, the inhomogeneity angle affects the energy partitions, particularly near grazing incidence, where the interference energy is enhanced for high inhomogeneity angles. Reflection dispersion mainly occurs at frequencies near the thermal relaxation frequency, which moves to low frequencies when the thermal conductivity increases.

In thermally insulated rocks, the temperature variation induced by the passage of *P* wave provides the gradient from which thermal dissipation and attenuation occur. The conversion from *P* wave to thermal wave induces energy transfer, causing wave-induced thermo-poroelastic attenuation of the fast *P* wave in analogy with wave-induced fluid-flow attenuation due to the conversion to Biot slow wave. The reflection dispersion due to thermo-poroelastic attenuation cannot be ignored because the classical Biot-type interpretation might be

misleading, particularly for high-temperature high-pressure fields. The approach can be generalized to the case of anisotropic thermo-poroelasticity in a future study.

ACKNOWLEDGEMENTS

We thank the Editors Fern Storey and Herve Chauris, the reviewer Junxin Guo and two anonymous reviewers, for their comments, which help improve the paper. This work has been supported by the 'National Natural Science Foundation of China (41804095)' and the 'China Postdoctoral Science Foundation (2020M682242)'. The related data and codes can be available by contacting the corresponding author.

REFERENCES

Anderson, O., 2000. The Grüneisen ratio for the last 30 years, *Geophys. J. Int.,* **143,** 279–294.

Ba, J., Carcione, J.M. & Nie, J., 2011. Biot-Rayleigh theory of wave propagation in double-porosity media, *J. geophys. Res.,* **116,** B06202, doi:10.1029/2010JB008185.

Ba, J., Xu, W., Fu, L., Carcione, J.M. & Zhang, L., 2017. Rock anelasticity due to patchy saturation and fabric heterogeneity: a double double–porosity model of wave propagation, *J. geophys. Res.,* **122**(3), 1949–1976.

Biot, M.A., 1956a. Theory of propagation of elastic waves in a fluid-saturated porous solid. I. Low frequency range, *J. acoust. Soc. Am.,* **28**(2), 168–178.

Biot, M.A., 1956b. Thermoelasticity and irreversible thermodynamics, *J. Appl. Phys.,* **27**(3), 240–253.

Biot, M.A., 1962. Mechanics of deformation and acoustic propagation in porous media, *J. Appl. Phys.,* **33**(4), 1482–1498.

Borcherdt, R.D., 1982. Reflection-refraction of general *P*-and type-I *S*-waves in elastic and anelastic solids, *Geophys. J. Int.,* **70**(3), 621–638.

Buchen, P.W., 1971. Plane waves in linear viscoelastic media, *Geophys. J. Int.,* **23**(5), 531–542.

Carcione, J.M., 2006. Vector attenuation: elliptical polarization, raypaths and the Rayleigh-window effect, *Geophys. Prosp.,* **54,** 399–407.

Carcione, J.M., 2014. *Wave Fields in Real Media: Theory and Numerical Simulation of Wave Propagation in Anisotropic, Anelastic, Porous and Electromagnetic Media,* 3rd edn, Elsevier.

Carcione, J.M. & Seriani, G., 2001. Wave simulation in frozen porous media, *J. Comput. Phys.,* **170,** 676–695.

Carcione, J.M., Santos, J.E., Ravazzoli, C.L. & Helle, H.B., 2003. Wave simulation in partially frozen porous media with fractal freezing conditions, *J. Appl. Phys.,* **94,** 7839–7847.

Carcione, J.M., Cavallini, F., Wang, E., Ba, J. & Fu, L., 2019a. Physics and simulation of wave propagation in linear thermoporoelastic media, *J. geophys. Res.,* **124**(8), 8147–8166.

Carcione, J.M., Wang, Z., Ling, W., Salusti, E., Ba, J. & Fu, L., 2019b. Simulation of wave propagation in linear thermoelastic media, *Geophysics,* **84**(1), T1–T11.

Carcione, J.M., Gei, D., Santos, J.E., Fu, L. & Ba, J., 2020. Canonical analytical solutions of wave-induced thermoelastic attenuation, *Geophys. J. Int.,* **221**(2), 835–842.

Deresiewicz, H., 1957. Plane waves in a thermoelastic solid, *J. acoust. Soc. Am.,* **29**(2), 204–209.

Deresiewicz, H., 1960. Effect of boundaries on waves in a thermoelastic solid: reflexion of plane waves from a plane boundary, *J. Mech. Phys. Solids,* **8**(3), 164–172.

Deresiewicz, H. & Rice, J.T., 1964. The effect of boundaries on wave propagation in a liquid-filled porous solid: V. Transmission across plane interface, *Bull. seism. Soc. Am.,* **54**(1), 409–416.

Dutta, N.C. & Odé, H., 1983. Seismic reflections from a gas–water contact, *Geophysics,* **48**(2), 148–162.

Green, A.E. & Lindsay, K.E., 1972. Thermoelasticity, *J. Elast.,* **2**(1), 1–7.

Guo, J. & Gurevich, B., 2020a. Effects of coupling between wave-induced fluid flow and elastic scattering on *P*-wave dispersion and attenuation in rocks with aligned fractures, *J. geophys. Res.,* **125**(3), e2019JB018685.

Guo, J. & Gurevich, B., 2020b. Frequency-dependent *P* wave anisotropy due to wave-induced fluid flow and elastic scattering in a fluid-saturated porous medium with aligned fractures, *J. geophys. Res.,* **125**(8), e2020JB020320.

Gurevich, B., Ciz, R. & Denneman, A.I.M., 2004. Simple expressions for normal incidence reflection coefficients from an interface between fluid-saturated porous materials, *Geophysics,* **69**(6), 1372–1377.

Ignaczak, J. & Ostoja-Starzewski, M., 2010. *Thermoelasticity with Finite Wave Speeds,* Oxford University Press.

Kumar, M. & Sharma, M.D., 2013. Reflection and transmission of attenuated waves at the boundary between two dissimilar poroelastic solids saturated with two immiscible viscous fluids, *Geophys. Prospect.,* **61**(5), 1035–1055.

Kumar, R. & Sarthi, P., 2006. Reflection and refraction of thermoelastic plane waves at an interface between two thermoelastic media without energy dissipation, *Arch. Mech.,* **58**(2), 155–185.

Liu, X., Greenhalgh, S. & Carcione, J.M., 2020a. Seismic *Q* of inhomogeneous plane waves in porous media, *Geophysics,* **85**(3), T209–T224.

Liu, X., Greenhalgh, S., Zhou, B., Ren, Z. & Li, H., 2020b. *Q* values and wave inhomogeneity parameters of reflected inhomogeneous *P* and *S* waves at the free surface of an effective Biot solid, *Geophys. J. Int.,* **222**(2), 919–939.

Lo, W.C., Sposito, G. & Majer, E., 2005. Wave propagation through elastic porous media containing two immiscible fluids, *Water Resour. Res.,* **41**(2), W02025, doi:10.1029/2004WR003162.

Lord, H. & Shulman, Y., 1967. A generalized dynamical theory of thermoelasticity, *J. Mech. Phys. Solids,* **15**(5), 299–309.

Markov, M., Markova, I. & Pervago, E., 2019. Reflection and transmission of elastic waves by a fluid-filled crack located in a poroelastic formation, *J. Appl. Geophys.,* **167,** 63–72.

Poletto, F., Farina, B. & Carcione, J.M., 2018. Sensitivity of seismic properties to temperature variations in a geothermal reservoir, *Geothermics,* **76,** 149–163.

Pride, S.R. & Berryman, J.G., 2003a. Linear dynamics of double porosity dual-permeability materials. I. Governing equations and acoustic attenuation, *Phys. Rev. E,* **68**(3), 036603, doi:10.1103/PhysRevE.68.036603.

Pride, S.R. & Berryman, J.G., 2003b. Linear dynamics of double porosity dual-permeability materials. II. Fluid transport equations, *Phys. Phys. Rev. E,* **68**(3), 036604, doi:10.1103/PhysRevE.68.036604.

Pride, S.R., Berryman, J.G. & Harris, J.M., 2004. Seismic attenuation due to wave-induced flow, *J. geophys. Res.,* **109,** B01201, doi:10.1029/2003JB002639.

Rubino, J.G., Ravazzoli, C.L. & Santos, J.E., 2006. Reflection and transmission of waves in composite porous media: a quantification of energy conversions involving slow waves, *J. acoust. Soc. Am.,* **120**(5), 2425–2436.

Rudgers, A.J., 1990. Analysis of thermoacoustic wave propagation in elastic media, *J. acoust. Soc. Am.,* **88**(2), 1078–1094.

Santos, J.E., Douglas, J., Jr, Corbero, J. & Lovera, O.M.A., 1990. A model for wave propagation in a porous medium saturated by a two phase fluid, *J. acoust. Soc. Am.,* **87**(4), 1439–1448.

Santos, J.E., Corbero, J.M., Ravazzoli, C.L. & Hensley, J.L., 1992. Reflection and transmission coefficients in fluid-saturated porous media, *J. acoust. Soc. Am.,* **91**(4), 1911–1923.

Santos, J.E., Ravazzoli, C.L. & Carcione, J.M., 2004. A model for wave propagation in a composite solid matrix saturated by a single-phase fluid, *J. acoust. Soc. Am.,* **115**(6), 2749–2760.

Sharma, J.N., Kumar, V. & Chand, D., 2003. Reflection of generalized thermoelastic waves from the boundary of a half-space, *J. Therm. Stresses,* **26**(10), 925–942.

Sharma, M.D., 2008. Wave propagation in thermoelastic saturated porous medium, *J. Earth Syst. Sci.,* **117**(6), 951–958.

Sharma, M.D., 2013. Effect of local fluid flow on reflection of plane elastic waves at the boundary of a double-porosity medium, *Adv. Water Resour.,* **61,** 62–73.

Sharma, M.D., 2018. Reflection-refraction of attenuated waves at the interface between a thermo-poroelastic medium and a thermoelastic medium, *Waves Random Complex Media,* **28**(3), 570–587.

Singh, B., 2007. Reflection coefficients and energy ratios in a micropolar thermoelastic medium without energy dissipation, *ANZIAM J.,* **48**(3), 433–447.

Singh, M.C. & Chakraborty, N., 2013. Reflection and refraction of *P*-, *SV*- and thermal wave, at an initially stressed solid–liquid interface in generalized thermoelasticity, *Appl. Math. Modelling,* **37**(1–2), 463–475.

Sinha, S.B. & Elsibai, K.A., 1996. Reflection of thermoelastic waves at a solid half-space with two relaxation times, *J. Therm. Stresses,* **19**(8), 749–762.

Tomar, S.K. & Arora, A., 2006. Reflection and transmission of elastic waves at an elastic/porous solid saturated by two immiscible fluids, *Int. J. Solids Struct.,* **43**(7–8), 1991–2013.

Wang, E., Carcione, J.M., Ba, J. & Liu, Y., 2020. Reflection and transmission of plane elastic waves at an interface between two double-porosity media: effect of local fluid flow, *Surv. Geophys.,* **41**(2), 283–322.

Wei, W., Zheng, R., Liu, G. & Tao, H., 2016. Reflection and refraction of *P* wave at the interface between thermoelastic and porous thermoelastic medium, *Transp. Porous Media,* **113**(1), 1–27.

Zhao, L., Han, D.H., Yao, Q., Zhou, R. & Yan, F., 2015. Seismic reflection dispersion due to wave-induced fluid flow in heterogeneous reservoir rocks, *Geophysics,* **80**(3), D221–D235.

APPENDIX A: COMPONENTS OF M AND y

The components of matrix **M** are

$$\begin{aligned}
&M_{11} = 2p_1q_1,\ M_{12} = 2p_2q_2,\ M_{13} = 2p_3q_3,\\
&M_{14} = (p_4^2 - q_4^2),
\end{aligned} \tag{A1}$$

$$\begin{aligned}
M_{21} &= (\lambda + \alpha^2 M + \alpha M \nu_1)(p_1^2 + q_1^2) + 2\mu q_1^2 + \frac{\beta\delta_1\bar{\tau}_1}{\omega^2},\\
M_{22} &= (\lambda + \alpha^2 M + \alpha M \nu_2)(p_2^2 + q_2^2) + 2\mu q_2^2 + \frac{\beta\delta_2\bar{\tau}_1}{\omega^2},\\
M_{23} &= (\lambda + \alpha^2 M + \alpha M \nu_3)(p_3^2 + q_3^2) + 2\mu q_3^2 + \frac{\beta\delta_3\bar{\tau}_1}{\omega^2},\\
M_{24} &= 2\mu p_4 q_4,
\end{aligned} \tag{A2}$$

$$\begin{aligned}
M_{31} &= \mathrm{i}\omega\vartheta\nu_1 q_1 - \omega^2(1-\vartheta)\left((\alpha M + M\nu_1)(p_1^2 + q_1^2) + \frac{\beta_f\delta_1\bar{\tau}_2}{\omega^2\phi}\right),\\
M_{32} &= \mathrm{i}\omega\vartheta\nu_2 q_2 - \omega^2(1-\vartheta)\left((\alpha M + M\nu_2)(p_2^2 + q_2^2) + \frac{\beta_f\delta_2\bar{\tau}_2}{\omega^2\phi}\right),\\
M_{33} &= \mathrm{i}\omega\vartheta\nu_3 q_3 - \omega^2(1-\vartheta)\left((\alpha M + M\nu_3)(p_3^2 + q_3^2) + \frac{\beta_f\delta_3\bar{\tau}_2}{\omega^2\phi}\right),\\
M_{34} &= \mathrm{i}\omega\vartheta\nu_4 p_4,
\end{aligned} \tag{A3}$$

$$\begin{aligned}
&M_{41} = q_1\delta_1,\\
&M_{42} = q_2\delta_2,\\
&M_{43} = q_3\delta_3,\\
&M_{44} = 0.
\end{aligned} \tag{A4}$$

The components of **y** are

$$\begin{aligned}
y_1 &= 2\sigma A_s^{(0)} p_0 q_0 - (1-\sigma)B_s^{(0)}(p_0^2 - q_0^2),\\
y_2 &= A_s^{(0)}\sigma\left(-(\lambda + \alpha^2 M + \alpha M\nu_0)(p_0^2 + q_0^2) - 2\mu q_0^2 - \frac{\beta\delta_0\bar{\tau}_1}{\omega^2}\right) + B_s^{(0)}(1-\sigma)2\mu p_0 q_0,\\
y_3 &= \sigma A_s^{(0)}\left[\mathrm{i}\omega\vartheta\nu_0 q_0 + \omega^2(1-\vartheta)\left((\alpha M + M\nu_0)(p_0^2 + q_0^2) + \frac{\beta_f\delta_0\bar{\tau}_2}{\omega^2\phi}\right)\right]\\
&\quad -(1-\sigma)B_s^{(0)}\mathrm{i}\omega p_0\vartheta\nu_0,\\
y_4 &= q_0\delta_0\sigma A_s^{(0)}.
\end{aligned} \tag{A5}$$